Structural Basis for the Functional Differences between Type I and Type II Human Methionine Aminopeptidases[†,‡]

Anthony Addlagatta,[§] Xiaoyi Hu,[||] Jun O. Liu,[||] and Brian W. Matthews*[,§]

Institute of Molecular Biology, Howard Hughes Medical Institute and Department of Physics, 1229 University of Oregon, Eugene, Oregon 97403-1229, and Department of Pharmacology and Molecular Sciences, Johns Hopkins School of Medicine, 725 North Wolfe Street, Baltimore, Maryland 21205

Received August 24, 2005; Revised Manuscript Received September 21, 2005

ABSTRACT: Determination of the crystal structure of human MetAP1 makes it possible, for the first time, to compare the structures of a Type I and a Type II methionine aminopeptidase (MetAP) from the same organism. Comparison of the Type I enzyme with the previously reported complex of ovalicin with Type II MetAP shows that the active site of the former is reduced in size and would incur steric clashes with the bound inhibitor. This explains why ovalicin and related anti-angiogenesis inhibitors target Type II human MetAP but not Type I. The differences in both size and shape of the active sites between MetAP1 and MetAP2 also help to explain their different substrate specificity. In the presence of excess Co^{2+}, a third cobalt ion binds in the active site region, explaining why metal ions in excess can be inhibitory. Also, the N-terminal region of the protein contains three distinct Pro-x-x-Pro motifs, supporting the prior suggestion that this region of the protein may participate in binding to the ribosome.

In eukaryotes all proteins synthesized in the cytosol are initiated by methionine, while in prokaryotes, mitochondria, and chloroplasts, they are initiated by formylated methionine (*1*−*3*). The formyl group is hydrolyzed by a deformylase. Methionine aminopeptidases (MetAPs)[1] remove the N-terminal methionine, which is essential for the maturation of many proteins (*4*). There are two classes of MetAPs, Type I and Type II, differentiated by a 60-amino acid insertion in the latter (Figure 1a). Type I is further divided into Type Ia, Type Ib, and Type Ic (*1*, *5*). Type Ia enzymes have only the catalytic domain, with the prototypical example being *Escherichia coli* MetAP (*Ec*MetAP). Type Ia and Type Ic MetAPs are present in prokaryotes, while Type Ib is present only in eukaryotes (*5*). Type Ib and Type Ic have, respectively, about 120 and 40 extra amino acids at their N-termini, of which the former has two zinc finger motifs at the extreme N-terminus connected by a 50-residue linker. Deletion of the zinc finger domain of yeast MetAP1 has no effect on catalytic activity in vitro, but results in a slow growth phenotype, suggesting that it is important for the function of the enzyme in vivo (*6*). Type II MetAP is found in eukaryotes and archea (*1*, *7*). Deletion of the MetAP genes from *E. coli*, *Salmonella typhimurium*, and *Saccharomyces cerevisiae* is lethal (*8*−*10*) indicating that these enzymes could serve as drug targets for antibiotics and antifungal agents.

Human MetAP2 has been identified as the primary target of fumagillin and ovalicin, natural products of fungal origin, which act as potent inhibitors of angiogenesis (*11*−*13*). A synthetic analogue of fumagillin, TNP-470 (also known as AGM-1470), with less toxicity and more potency, has undergone clinical trials for a variety of cancers. This family of compounds inhibits MetAP2 by covalently modifying a histidine residue (*12*−*15*), which is conserved in both MetAP1 and MetAP2 (Figure 1b). Determination of the crystal structures of MetAP2 in complex with fumagillin (*15*) has suggested the mechanisms for drug inhibition. Despite the homology of catalytic domains between both MetAPs, little is known about the mechanism of drug selectivity for MetAP1.

We describe here the structure of human MetAP1 that includes the catalytic domain and a connector region which is absent in human MetAP2 (Figure 1a). The zinc finger region had to be removed to permit crystallization. In addition to the two-cobalt "native" enzyme structure, we also determined the structure of a trimetallo form of MetAP1 in which a third cobalt ion is coordinated by a conserved histidine side chain within the active site. Comparison of the active sites of MetAP1 and MetAP2 reveals a smaller pocket in the former protein with more steric restrictions, which suggest that limited accessibility is responsible for fumagillin specificity toward MetAP2, and different substrate specificity.

EXPERIMENTAL PROCEDURES

Cloning, Expression, and Purification. Truncated *Hs*MetAP1 (Δ1−89) was amplified from the full-length

[†] This work was supported in part by NIH Grants GM20066 to B.W.M. and CA078743 to J.O.L., and Keck Center support to J.O.L.

[‡] PDB Codes: 2B3H, 2B3K, and 2B3L.

* Corresponding author. E-mail: brian@uoxray.uoregon.edu. Phone: (541) 346-2572. Fax: (541) 346-5870.

[§] Institute of Molecular Biology, Howard Hughes Medical Institute and Department of Physics, University of Oregon.

[||] Department of Pharmacology and Molecular Sciences, Johns Hopkins School of Medicine.

[1] Abbreviations: MetAP, methionine aminopeptidase; *Hs*MetAP1, Type I human MetAP; t*Hs*MetAP1, truncated Type I human MetAP; *Hs*MetAP2, Type II human MetAP; *Mt*MetAP1c, *Mycobacterium tuberculosis* MetAP; *Sa*MetAP1, Type I *Staphylococcus aureus* MetAP; SH3, Src homology domain 3; PxxP, polyproline motif.

10.1021/bi051691k CCC: $30.25
Published on Web 10/22/2005

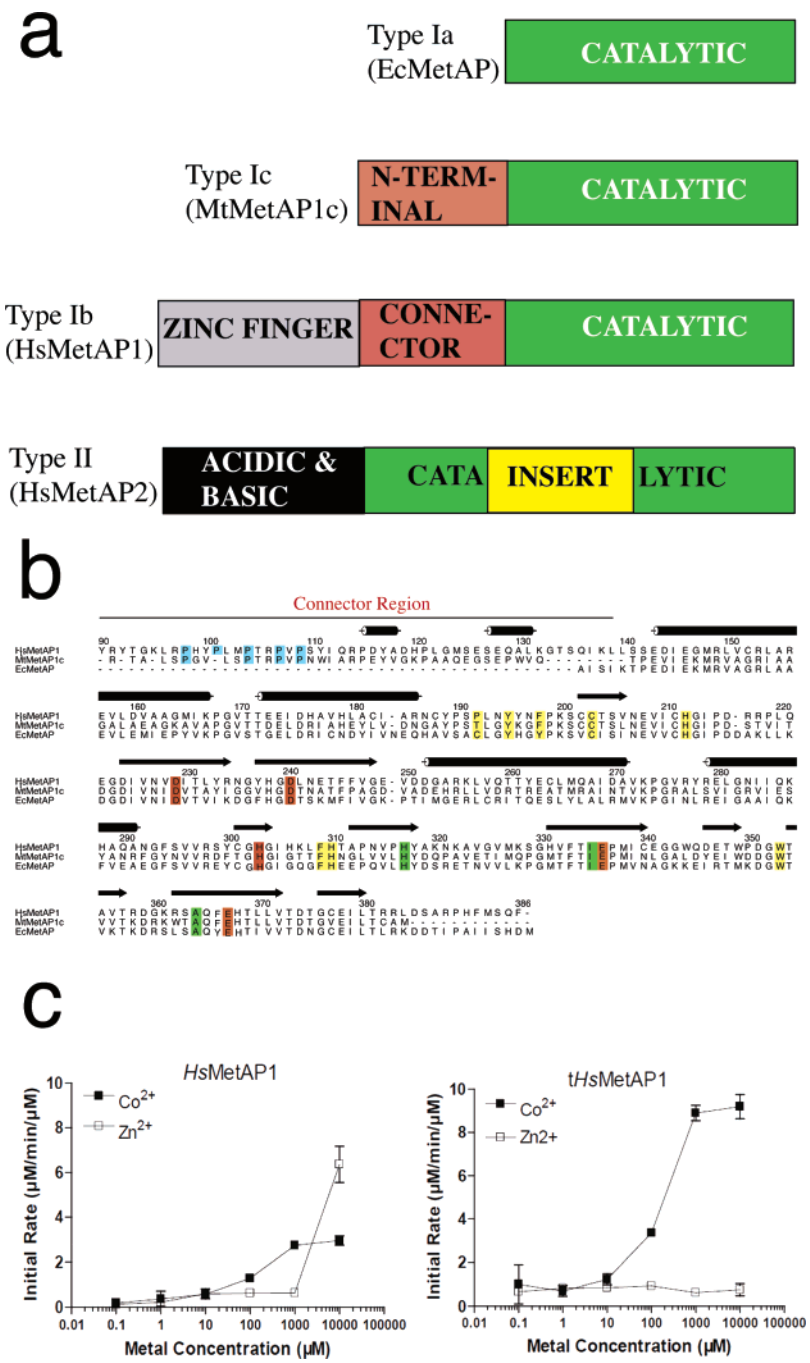

FIGURE 1: (a) Domain organization of Type I and Type II MetAPs. From top to bottom, the representative enzymes named in parentheses are from *E. coli*, *M. tuberculosis*, human (Type I), and human (Type II). (b) Sequence alignment of *Hs*MetAP1, *Mt*MetAP1c, and *Ec*MetAP. The secondary structures and the numbering above the sequences are from *Hs*MetAP1 (this work). Prolines in the connector region are shown in blue. The metal-binding residues are boxed in red, while residues that form the S1 and S1′ substrate-binding subsites are colored yellow and green, respectively. (c) Activation of full-length *Hs*MetAP1 and truncated t*Hs*MetAP1 by divalent ions: Co(II) (filled squares) and Zn(II) (open squares).

cDNA (in the pGEX-2T vector) with introduction of NdeI and BamHI restriction sites. The sequence of the primers for PCR amplification was forward, 5′-GGAATTCCATATGCCATATCGATATACTGGTAAACTCAGACC, and reverse, 5′-CGAGGATCCTTAAAATTGAGACATGAAGTGAGGCC. An internal NdeI site at nucleotide 783 was modified to a silent mutation by site-directed mutagenesis (primers: forward, 5′-GCTTGCATCAGGCACTCGTATGTGGTCTGAACAAGTTTCC, and reverse, 5′-GGAAACTTGTTCAGACCACATACGAGTGCCTGATGCAAGC). The PCR product was cloned into pET15b vector (Novagen) with an N-terminal His-tag and thrombin protease site (a total of 21 amino acids). The final clone was transformed into BL21 (DE3) expression cells (Stratagene). Two liters of LB media were incubated at 37 °C with 100 mL of overnight culture while shaking at 250 rpm. At $OD_{600} = 1.5$, the temperature was reduced to 25 °C and the culture induced with 1 mM IPTG and further incubated for 8 h while shaking at 150 rpm. Cells were harvested by centrifuging at 5000*g* and stored at −80 °C.

Frozen cell pellet was re-suspended in +T/G buffer (50 mM HEPES, pH 8.0, 0.5 M KCl, 10% glycerol, 0.1% Triton

X-100, and 5 mM imidazole). All subsequent procedures were at 4 °C. Two tablets of EDTA-free protease cocktail inhibitors (Boehringer Mannheim), 1 mL of 1 M $MgCl_2$, and 5 mg of DNAse I (Sigma) were added. After complete resuspension, cells were lysed by passing twice through a French press. Cell debris was cleared by centrifugation at 15 000*g* for 30 min. The supernatant was loaded onto a Talon column (cobalt affinity resin, BD Biosciences). Continued application of +T/G buffer was used to wash the column until the absorption at 280 nm reached the baseline. The column was further washed with −T/G buffer (50 mM HEPES, pH 8.0, 0.5 M KCl, and 5 mM imidazole). Pure protein was eluted using −T/G buffer plus 100 mM imidazole directly into a flask containing 1 mL of 0.5 M EDTA, pH 8.0. A total of 50 mL of elutant was collected with a concentration of 9 mg/mL (determined by absorption at 280 nm with estimated extinction coefficient of 34 990 M^{-1} cm^{-1}) yielding a total of about 450 mg of pure protein (single band on the SDS−PAGE gel) from a 2 L culture. Mass spectroscopic analysis by matrix-assisted laser desorption ionization-time-of-flight (MALDI-TOF) showed a single symmetrical peak centered at 36 625 ± 45 (expected, 36 667.6). Protein was dialyzed into storage buffer (25 mM HEPES, pH 8.0, 5 mM methionine, and 150 mM KCl). During dialysis, part of the protein precipitated and was removed by centrifugation. The protein was concentrated to 30 mg/mL, divided into aliquots, frozen in liquid nitrogen, and stored at −80 °C until further use. No attempts were made to cleave the His-tag or purify further.

Enzyme Activity Assays. The assay was performed at room temperature on a 96-well clear polystyrene microplate. In the metal-dependence experiment, each well contained a 100 μL mixture of 40 mM HEPES (pH 7.5), 100 mM NaCl, 1 mM Met-Pro-*p*-NA, 1 unit/mL ProAP (reaction volume = 100 μL), 200 nM *Hs*MetAP1 or t*Hs*MetAP1, and various concentrations of metal ions ($CoCl_2$, $MnCl_2$, $ZnCl_2$, or $NiCl_2$). The production of *p*-NA was monitored continuously by absorbance at 405 nm ($\epsilon_{405nm} = 1.06 \times 104$ M^{-1} cm^{-1}) (*16*). The initial rate of hydrolysis was determined using the early linear portion of the enzymatic reaction curve, subtracting the background hydrolysis.

To obtain the kinetic constants using Met-Pro-*p*-NA, the reaction was performed in a 100 μL mixture containing 40 mM HEPES, pH 7.5, 100 mM NaCl, 100 μM $CoCl_2$, 1 unit/mL ProAP, 200 nM *Hs*MetAP1 or t*Hs*MetAP1, and Met-Pro-*p*-NA in 2-fold dilutions up to 20 mM. The plates were read on a SpectraMax Plus microplate reader from Molecular Devices, and the initial rate was calculated from the early part (<5 min) of the reaction curve. The k_{cat} and K_m values of *Hs*MetAP1 and t*Hs*MetAP1 were derived by nonlinear regression curve-fitting using the Michaelis−Menten equation from GraphPad Prism 4 software.

Crystallization. Protein stored at −80 °C was thawed and diluted to 10 mg/mL in the storage buffer. Initial crystallization conditions were determined by using Index screen (Hampton Research) in 96-well-sitting drop plates (Hampton Research) at room temperature. Final crystallizations were performed at 25 °C by the hanging-drop vapor-diffusion method. Each drop contained 5 μL of the protein and 5 μL of the reservoir solution (4−6% PEG 10 000 or 12−16% PEG monomethyl ether 2000, in 100 mM HEPES, pH 5.4−6.2). In the absence of metals, rodlike crystals appeared in 12−16 h, continued to grow for 3 days, and diffracted to high resolution. In the presence of metals [Mn(II), Fe(II), Co(II), Ni(II), or Zn(II)] the protein tended to precipitate and no useful crystals were obtained. The apocrystals were, however, stable when soaked with any of the above divalent cations. The largest crystals of the apoprotein were 0.1 mm × 0.1 mm × 0.8 mm.

Table 1: X-ray Data Collection and Refinement Statistics[a]

	apo	holo (two Co(II))	trimetallo (three Co(II))
Space group	$P2_1$	$P2_1$	$P2_1$
Cell parameters			
a (Å)	47.22	47.43	47.29
b (Å)	77.28	77.52	77.30
c (Å)	47.85	48.31	48.34
β (deg)	91.58	90.60	91.03
X-ray data collection			
resolution range (Å)	20−1.5 (1.55−1.5)	20−1.55 (1.61−1.55)	20−1.1 (1.12−1.1)
collected reflections	915 351	773 240	2 112 709
unique reflections	51 841 (4470)	47 891 (4003)	255 244 (9989)
completeness (%)	96.1 (82.3)	95.6 (79.9)	91.8 (72.7)
$\langle I/\sigma(I)\rangle$	37.6 (7.5)	18.8 (1.9)	30.1 (4.2)
R_{sym} (%)	3.1 (10.9)	3.9 (39.7)	3.1 (16.9)
Refinement statistics			
R (%)	12.2	19.2	10.1
R_{free} (%)	18.0	21.7	13.1
Δ_{bonds} (Å)	0.01	0.02	0.01
Δ_{angles} (deg)	0.03	0.03	0.03
PDB codes	2B3L	2B3K	2B3H

[a] Numbers given in parentheses correspond to the highest-resolution shell of data.

To obtain the two-cobalt (i.e., holo) form, freshly prepared $CoCl_2$ in water was added to give a final concentration of 1−5 mM and incubated for 2−24 h. Crystals were then soaked for 5 min in the cryoprotectant solution (6% PEG 10 000 or 16% PEG monomethyl ether 2000, 25% glycerol, and 100 mM HEPES, pH 6.0) and flash-frozen either directly in liquid nitrogen or at 100 K in a stream of nitrogen gas. Diffraction data were also collected for crystals soaked for 1 day in the presence of about 50 molar equivalents of $CoCl_2$ (i.e., the tri-cobalt form) and were swept once through cryoprotectant (no cobalt) before freezing. These crystals diffracted synchrotron radiation to a resolution of 1.1 Å (Table 1).

Data Collection and Processing. X-ray diffraction data (Table 1) were collected at the Advanced Light Source (ALS) on BL8.2.1 for the apo and holo forms and on BL8.2.2 for the trimetallo form. Data processing and scaling were performed with HKL2000 and SCALEPACK (*17*).

Structure Determination and Refinement. The structure of the holo form was determined by molecular replacement using the program EPMR (*18*). Coordinates of *Mt*MetAP1c (PDB: 1YJ3; truncated to poly-alanine with all metal ions and water molecules removed) were used as the starting model (*5*). Rigid-body refinement and simulated annealing with CNS (*19*), followed by iterative refinement and model building (*19*, *20*) were used to obtain the final model. These coordinates, without water and metal ions, were then used as starting molecular replacement models for the apo and trimetallo forms. As before, refinement included simulated annealing and repeated cycles of positional and *B*-factor refinement. When the *R*-factor stopped decreasing, refinement was shifted to SHELX (*21*). After conjugate-gradient

least-squares refinement and model checking, refinement with anisotropic thermal factors was launched. In the final stages, hydrogen atoms were introduced and some of the restraints on the main chain were relaxed. Final refinement statistics are summarized in Table 1. An apparent metal ion in the cradle formed by the tight turn between residues 205−209 was identified as potassium ion at full occupancy. In all three structures, this ion has *B*-factors that are comparable to those of the coordinating atoms.

Sequence and structural alignments were performed using SEQUOIA (*22*) and LSQMAN (*23*). Figures were generated by ALSCRIPT (sequence alignment) (*24*), MOLSCRIPT (*25*), and PyMol (*26*).

RESULTS AND DISCUSSION

Design of the Expression Construct. Repeated attempts to crystallize full-length *Hs*MetAP1 did not yield diffraction-quality crystals. Comparison with the recently determined structure of Type 1c *Mycobacterium tuberculosis* MetAP (*Mt*MetAP1c) (*5*) suggested that the Δ1−89 truncation might behave better. *Mt*MetAP1c has an N-terminal extension of 40 amino acids (Figure 1a) that is wrapped around the catalytic domain. This N-terminal extension has about 48% sequence homology with the connector region of *Hs*MetAP1 (Figure 1b). Recently, Li et al. (*27*) have shown that the Δ1−75 truncation mutant, which lacks the zinc finger motifs (Figure 1a), is stable and enzymatically active. In contrast, the Δ1−144 mutant that deletes the connector region is unstable and less active. This suggests that the connector region is an integral part of the catalytic domain.

The full-length protein (*Hs*MetAP1) was prepared with an N-terminal GST-tag from pGEX-2T and overexpressed in *E. coli* BL21 (DE3) strain. Single-step GST-sepharose affinity chromatography generated nearly homogeneous protein as judged by Coomassie Blue staining. The GST-tag was subsequently removed by thrombin cleavage. The Δ1−89 mutant (t*Hs*MetAP1) clone was prepared with an N-terminal His-tag in pET15b and overexpressed in *E. coli* BL21 (DE3) strain. There was a high level of expression, and single-step metal affinity chromatography yielded nearly homogeneous protein as judged by silver-stained SDS−PAGE.

The kinetic properties of full-length and truncated proteins were studied with a prolyl aminopeptidase (ProAP)-coupled spectrophotometric reaction using Met-Pro-*p*-nitroanilide as a substrate (*16*). Although methionine aminopeptidases have been characterized as Co(II) enzymes (*4*), their physiological metal ions remain elusive (*28*, *29*). In this study, both the full-length and truncated proteins can be activated by Co(II), whereas neither protein is activated by Mn(II) or Ni(II) (data not shown). Interestingly, a high concentration of Zn(II) is able to activate only the full-length protein (Figure 1c). Kinetic constants have been determined for both proteins. t*Hs*MetAP1 was found to cleave the Met-Pro-*p*-NA substrate more efficiently with a slightly increased K_m and significantly increased k_{cat} (Table 2). These results suggest that the N-terminal 89 amino acid region is not essential for catalytic activities, but its existence does change the efficiency in hydrolysis and metal selectivity as compared with full-length protein.

Overall Structure. We determined three different structures of t*Hs*MetAP1, the apoenzyme, the holoenzyme with two cobalt in the active site, and a third form with a third cobalt bound to the enzyme. Except for the last two residues at the C-terminus, all residues of t*Hs*MetAP1 could be built into electron density in all three structures.

Table 2: Kinetic Constants of Truncated and Full-Length Human MetAP1 in Hydrolyzing Met-Pro-*p*-NA

	K_m (mM)	k_{cat} (min^{-1})	k_{cat}/K_m ($M^{-1}\,min^{-1}$)
t*Hs*MetAP1	1.8 ± 0.13	25.5 ± 0.9	14 167
*Hs*MetAP1	0.74 ± 0.08	6.7 ± 0.2	9114

The catalytic domain of t*Hs*MetAP1 adopts the usual pita-bread fold for this family of enzymes. All the residues in the active site that coordinate the metal ions are conserved in sequence and structure. The connector region forms a rooflike structure "above" the active site, which is a feature that has no precedence in other Type I MetAPs. As expected, the metal-binding site is negatively charged, and the methionine side chain binding pocket is hydrophobic (not shown). There is also a large patch of positively charged surface adjacent to the active site.

Within the catalytic domain, *Hs*MetAP1 has 49% sequence identity with *Mt*MetAP1c and 47% with *Ec*MetAP. The root-mean-square deviations (rmsd) of C^{α} coordinates with *Mt*MetAP1c (PDB: 1YJ3) and *Ec*MetAP (PDB: 1C21) are 0.95 Å and 0.87 Å, respectively. The connector region wraps around the catalytic domain making a number of specific contacts as seen with *Mt*MetAP1c (*5*). Almost all the residues in the S1 and S1′ subsites are conserved (Figure 1b).

The N-terminal extensions in *Mt*MetAP1c and t*Hs*MetAP1 have overall similar traces. However, some differences were observed in the structure of the connector region (Figure 2a). t*Hs*MetAP1 has an insertion of about eight amino acids in the vicinity of residues 130−140 compared to *Mt*MetAP1c (Figure 1b). This is associated with changes in conformation including the presence of two short α-helices that were not seen in *Mt*MetAP1c (Figure 2a). Notwithstanding the structural and sequence changes in this region, there are two spatially conserved residues (Tyr117 and Glu128 in *Hs*-MetAP1 and Tyr27 and Glu35 in *Mt*MetAP1c) which form hydrogen bonds and hydrophobic interactions with residues that help form the substrate-binding pocket (Ser191, Tyr195, Phe309, and His310 in human and Ser93, Tyr97, and Phe211 in *Mt*MetAP1c) (Figure 2b). In addition to these interactions, Ile112, Tyr117, His120, Gly123, and Met124 in the connector region make either polar or nonpolar interactions with the active site residues Cys188, Ser191, Asn194, and Tyr196, suggesting that the connector region is important in defining the specificity of the active site.

There was no electron density for any of the extra residues at the N-terminus, which are part of the His-tag and the thrombin recognition site. Clear electron density started with Tyr90, which is the first residue of t*Hs*MetAP1, indicating that the design of the truncation site was appropriate. The side chain of Tyr90 extends into a cavity and interacts with Glu347, Tyr92, and Pro350 (Figure 3a). Refinement of the structure revealed an apparent glycerol molecule bound within a relatively deep pocket in the surface of the protein. This pocket is formed by residues 204−219 of the catalytic domain together with residues 97−99 of the connector region. Although one of the terminal hydroxyl groups is in

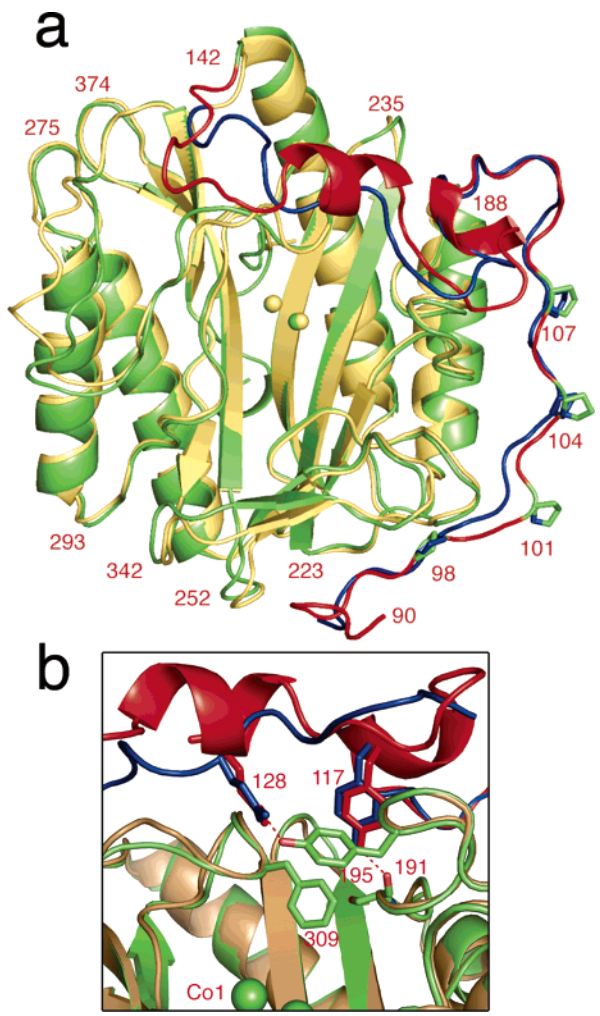

FIGURE 2: (a) An overlay of the crystal structures of t*Hs*MetAP1 (catalytic domain in green and the N-terminal extension in red) and *Mt*MetAP1c (gold and blue). The numbering throughout is based on *Hs*MetAP1, and the prolines in the PxxP motifs are at residues 98, 101, 104, and 107. (b) Structural alignment of the connector regions of t*Hs*MetAP1 (red) and *Mt*MetAP1c (blue). Tyr117 and Glu128 from the human enzyme, and the corresponding Tyr27 and Glu35 of *Mt*MetAP1c, have different structural environments but interact with similar residues in the methionine-binding pocket. For the sake of clarity, only the pocket of t*Hs*MetAP1 is shown.

two conformations, the glycerol molecule is very well-ordered with all of its hydrogen-bond potential satisfied (Figure 3b). The source of the glycerol is presumably the cryoprotectant used to freeze the crystals.

Apo and Holo tHsMetAP1. The structural features observed in the active site of the holo form are similar to those found in other members of the MetAP family. Ligands around Co1 assume trigonal bipyramidyl geometry, while ligands around Co2 assume distorted octahedral geometry. These ligands are contributed by the conserved residues Asp229, Asp240, His 303, Glu336, and Glu367, a water molecule, and a second bridging water molecule or μ-hydroxo anion. In all three structures, some electron density was seen in the hydrophobic region that binds the side chain of the methionine substrate. This density is not in bonding distance to any of the active site residues. An anomalous scattering difference map for the apo structure did not show any indication of a metal ion in the active site. Also, the apoprotein did not show any catalytic activity unless fresh cobalt ion was added. The apo and holo forms are essentially identical apart from small differences in the conformations of the metal-binding residues. The rmsd of 0.15 Å between the C^{α} coordinates of the two structures is essentially equal to the estimated experimental error.

Trimetallo tHsMetAP1. An anomalous Fourier map for the structure in the presence of excess cobalt ion (Figure 4) showed peaks for Co1 and Co2 plus another density feature within the active site region. This map, together with subsequent refinement, suggested that a third cobalt ion (Co3) is bound in two alternative sites, one with about 50% occupancy and the other about 20%. The geometry around the higher-occupancy site is octahedral with one of the axial positions occupied by $N^{\epsilon 2}$ of His212 (2.2 Å). At the other axial position, diffuse but strong positive electron density in an ($F_o - F_c$) map was best modeled by a partially occupied chloride ion. Two of the equatorial ligands are water molecules (both 2.2 Å). The other two ligands (2.2 Å and 2.1 Å) are contributed by an apparent poorly ordered glycerol molecule. The holo and trimetallo structures again are essentially identical within experimental error with an overall rmsd of 0.12 Å for the C^{α} atoms.

Crystal structures of two inhibitor complexes for each of *Staphylococcus aureus* MetAP1 (*Sa*MetAP1) and *E. coli* MetAP have been reported recently in which a third metal ion is bound to the same histidine as in *Hs*MetAP1. In the *Sa*MetAP1 complexes, the third metal center has tetrahedral geometry, while in the case of *Ec*MetAP, it was octahedral (*30*, *31*). Luo et al. (*32*) have discovered non-peptide inhibitors that inhibit the enzyme in the nanomolar range in vitro but are less effective in vivo. The crystal structure of one of these inhibitors with *Ec*MetAP revealed that they utilize a third metal ion (*32*). Because the concentration of metal ions in living cells is low, inhibitors whose activity is mediated by transition metals may be compromised (*31*).

It is well-known that excess metal ions can inhibit metallopeptidases. The present result, together with earlier structural studies of thermolysin (*33*), suggests that this occurs because the excess ions tend to bind in the active site.

Comparisons between the Type I and II Methionine Aminopeptidases. The overall relationship between the structures of Type I and Type II human MetAP is illustrated in Figure 5a. The catalytic domains, with only 27% sequence identity, however, have very similar structures. All the metal-binding residues in the active site are conserved, whereas almost all of the residues that form the methionine-binding pocket are different. Notwithstanding these differences, the shape of the pocket is conserved.

The so-called insert region of Type II human MetAP (Figure 1a) forms a compact helical domain that contacts the catalytic domain in some of the same area covered by the connector of the Type I protein (Figure 5a). This may suggest a common functional role.

The anti-angiogenic compounds fumagillin, ovalicin, and TNP-470 have been shown to bind Type II but not Type I human MetAP. The structure of ovalicin in complex with the Type II enzyme has been described along with the holoenzyme (*15*). When the structure of t*Hs*MetAP1 is superimposed on that of the *Hs*MetAP2 complex with ovalicin, the rmsd for the 85 core C^{α} atoms (i.e., the atoms that surround the active site) is 1.1 Å. Details of this

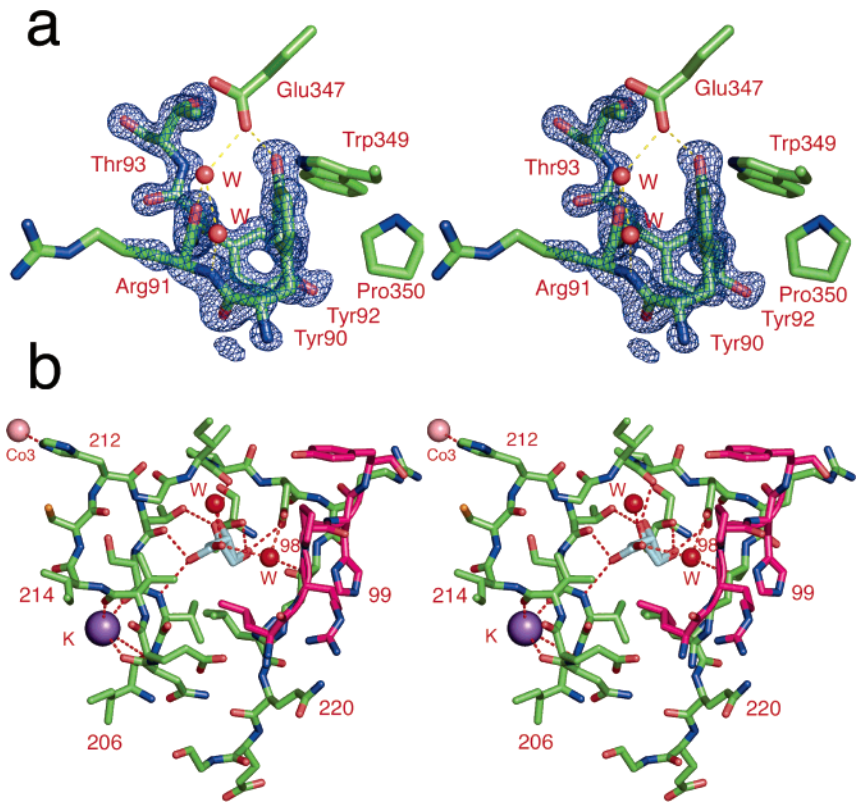

FIGURE 3: (a) Crystal structure of t*Hs*MetAP1 N-terminal region. The sequence of *Hs*MetAP1 included in the construct ends at Tyr90, and this is the terminal residue seen in the electron density map. An additional 21 residues are present as part of the expression vector, but none of these are seen. Superimposed is an "omit" electron density map shown in the vicinity of residues 90−93. Coefficients are $(F_o - F_c)$, where F_o are the observed structure amplitudes. The calculated amplitudes F_c and the phases were obtained from the refined model with residues 90−93 removed. The map is calculated at 1.1 Å resolution and contoured at 3.8 σ. (b) Stereo drawing showing the glycerol-binding pocket. The ligand, shown in light blue in two alternative conformations, forms a network of hydrogen bonds involving the main chain and side chains of the protein along with two well-ordered water molecules. Some of the residues that form part of the binding site are from the connector region (colored magenta) and include Pro98. Some residues that hydrogen-bond with the glycerol are also involved in potassium ion coordination (purple sphere).

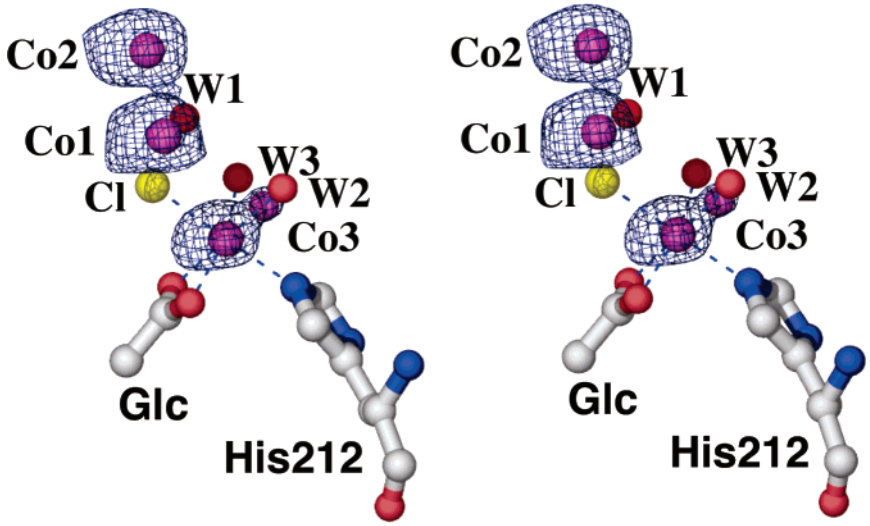

FIGURE 4: Stereo drawing of an anomalous difference map confirms binding at the Co1 and Co2 sites and also reveals the presence of a third Co3-binding site. The coordination of Co3 in its major binding location appears to be octahedral and includes a presumed chloride ion (Cl) and a disordered glycerol molecule (Glc). Amplitudes for the map are $(F^+ - F^-)$, where $(F^+ - F^-)$ is the Bijvoet difference for the trimetallo crystals. Phases are from the refined structure of the trimetallo protein with all cobalt ions removed from the model. Resolution is 1.1 Å, and the map is contoured at 6 σ.

superposition are shown in Figure 5b. In the *Hs*MetAP2 structure, it is His231 that covalently binds ovalicin. The conserved His212 residue in *Hs*MetAP1 shows similar orientation but has withdrawn about 1.1 Å from the active site. If ovalicin were bound to t*Hs*MetAP1 in the same position that it binds to *Hs*MetAP2, there would be several steric clashes, most significantly with His310 (Figure 5b) of *Hs*MetAP1. The corresponding His339 of *Hs*MetAP2 avoids the steric clash by adopting an alternative side-chain rotamer. His310 of t*Hs*MetAP1 could, in principle, do the

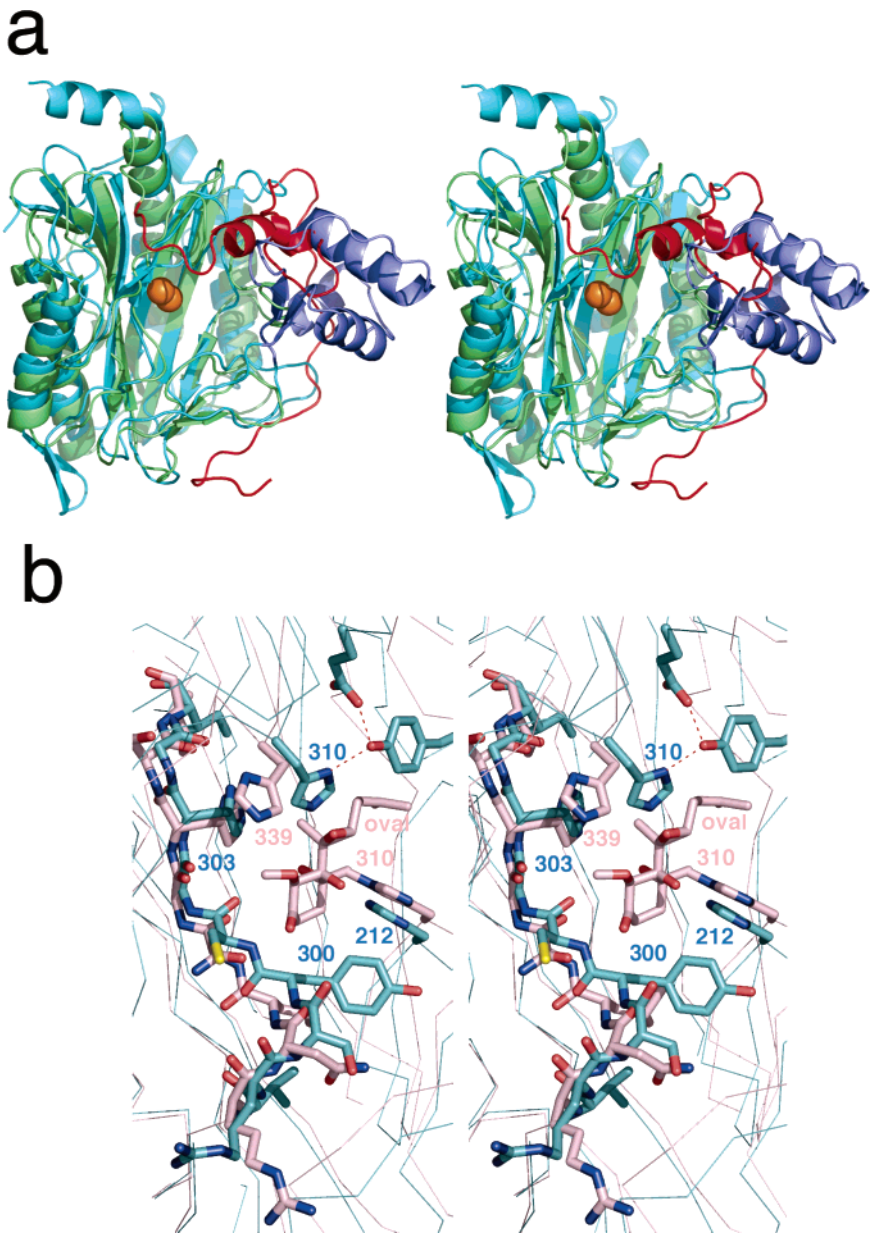

FIGURE 5: (a) Stereo diagram showing the relationship of t*Hs*MetAP1 (green) and *Hs*MetAP2 (cyan) structures. The catalytic domains are very similar. The connector region of t*Hs*MetAP1 (red) and the insert domain (blue) of *Hs*MetAP2 are located in similar regions on the surface of the catalytic domains. (b) Stereo diagram comparing the holo form of the t*Hs*MetAP1 (green) with the ovalicin-bound structure of *Hs*MetAP2 (PDB: 1B59, pink). Ovalicin, shown in pink, binds to *Hs*MetAP2 via a covalent bond to His310.

same, but it would require the loss of a hydrogen bond with Tyr195 (2.9 Å). In *Hs*MetAP2, the counterpart of Tyr195 is Met215, suggesting that no such hydrogen bond occurs. Another significant difference is that residues 298−303 of t*Hs*MetAP1 move ~1 Å "into" the active site. This has the effect of reducing the size of the active site and its entrance tunnel (Figure 5c). It would also tend to restrict accessibility of ovalicin to the active site of the Type I enzyme. In general, the relationship between the active sites of Type I and Type II human MetAPs seen here agrees quite well with that predicted from a comparison of Type II human MetAP with *E. coli* MetAP (a Type I enzyme) (*15*). Both studies suggest that there are a number of residues that would restrict access of ovalicin and related compounds to the active site of *Hs*MetAP1, explaining their reduced affinity for this enzyme.

Recently, Brdlik and Crews (*34*) showed that the single amino acid substitution, A362T, rendered *Hs*MetAP2 resistant to ovalicin. The corresponding inverse mutation in *Hs*MetAP1, T334A, made this enzyme sensitive to the inhibitor. In both enzymes, the residue that is the site of substitution interacts with a β-strand that forms part of the active site cleft. The interactions, however, are different. In *Hs*MetAP1, $O^{\gamma 1}$ of Thr334 forms a hydrogen bond with the main-chain nitrogen of His303, one of the active site metal-binding residues to the adjacent β-strand, but in *Hs*MetAP2, it is the backbone carbonyl of Ala362 that makes the analogous interaction with His331. Perhaps in association with this change, the segment of β-sheet (residues 298−303) protrudes into the active site about 1 Å more in *Hs*MetAP1 than the corresponding strand in *Hs*MetAP2 (residues 326−329) (Figure 5b). Whether the A362T mutation in *Hs*MetAP2 actually drives this conformational change and thereby restricts access to the active site (or vice versa for T334A in *Hs*MetAP1) needs to be tested experimentally.

The recently reported structure of *M. tuberculosis* MetAP (*5*) provided the first example of a MetAP with a structured extension at the amino-terminus (Figure 1a). Within this extension, there is a sequence element Pro-Thr-Arg-Pro (i.e., a PxxP motif) that is arranged on the surface of the protein in such a way that it seems poised to bind an SH3 protein domain. This led to the suggestion that the PxxP motif of *M. tuberculosis* MetAP might be the target site for mediating MetAP binding to ribosome (*5*). A prediction of this model is that MetAPs that bind to ribosomes should have an N-terminal extension and that this extension should include an appropriately placed PxxP motif. It has not been shown directly that human Type I MetAP binds to ribosome, but the protein does include an N-terminal extension. As shown in Figures 1b and 2a, this region of *Hs*MetAP1 includes not only a single PxxP motif but actually three motifs in tandem ($P_{98}xxP_{101}xxP_{104}xxP_{107}$). The $P_{104}xxP_{107}$ motif spatially aligns with $P_{14}xxP_{17}$ of the *M. tuberculosis* enzyme (Figure 2a). The motif $P_{101}xxP_{104}$ of the human enzyme also seems appropriately poised to bind an SH3 domain. In the case of $P_{98}xxP_{101}$, however, Pro_{98} turns inward and seems inaccessible for binding. It is possible, however, that $P_{98}xxP_{101}$ is also capable of interacting with an SH3 protein domain upon conformational changes. The presence of the multiple PxxP motifs may allow MetAP1 to associate with the ribosome in more than one configuration for optimal processing of different substrates. In summary, the present structure determination strongly supports the hypothesis that PxxP motifs within the N-terminal extension of MetAPs may be important for protein−protein interactions.

Significance. The structure of truncated but active human Type I methionine aminopeptidase has been determined. Comparison with the active site of human Type II methionine aminopeptidases reveals the structural basis for the differential inhibition by fumagillin and related anti-angiogenic drugs. One reason is the smaller active site pocket of the Type I enzyme, which limits accessibility. A second reason is that inhibitor binding to *Hs*MetAP1 requires ∼120° rotation of His310 and disruption of hydrogen bonding to Tyr195. In *Hs*MetAP2, a histidine (His339) undergoes a related conformational change (*15*), but there is no loss of hydrogen bonding. Insights from this investigation will also be useful in structure-based design of inhibitors specific for different methionine aminopeptidases.

ACKNOWLEDGMENT

We thank Leslie Gay for help with the cloning of t*Hs*MetAP1. Also, the use of beamlines BL8.2.1 and BL8.2.2 at the Advanced Light Source for X-ray data collection is gratefully acknowledged.

REFERENCES

1. Bradshaw, R. A., Brickey, W. W., and Walker, K. W. (1998) N-terminal processing: the methionine aminopeptidase and N alpha-acetyl transferase families, *Trends Biochem. Sci. 23*, 263−267.
2. Bradshaw, R. A., and Yi, E. (2002) Methionine aminopeptidases and angiogenesis, *Essays Biochem. 38*, 65−78.
3. Meinnel, T., Mechulam, Y., and Blanquet, S. (1993) Methionine as translation start signal: a review of the enzymes of the pathway in *Escherichia coli*, *Biochimie 75*, 1061−1075.
4. Ben-Bassat, A., Bauer, K., Chang, S. Y., Myambo, K., Boosman, A., and Chang, S. (1987) Processing of the initiation methionine from proteins: properties of the *Escherichia coli* methionine aminopeptidase and its gene structure, *J. Bacteriol. 169*, 751−757.
5. Addlagatta, A., Quillin, M. L., Omotoso, O., Liu, J. O., and Matthews, B. W. (2005) Identification of an SH3 binding motif in a class of methionine aminopeptidase from *Mycobacterium tuberculosis* suggests a mode of interaction with the ribosome, *Biochemistry 44*, 7166−7174.
6. Zuo, S., Guo, Q., Ling, C., and Chang, Y. H. (1995) Evidence that two zinc fingers in the methionine aminopeptidase from *Saccharomyces cerevisiae* are important for normal growth, *Mol. Gen. Genet. 246*, 247−253.
7. Lowther, W. T., and Matthews, B. W. (2002) Metalloaminopeptidases: common functional themes in disparate structural surroundings, *Chem. Rev. 102*, 4581−4608.
8. Chang, S. Y., McGary, E. C., and Chang, S. (1989) Methionine aminopeptidase gene of *Escherichia coli* is essential for cell growth, *J. Bacteriol. 171*, 4071−4072.
9. Miller, C. G., Kukral, A. M., Miller, J. L., and Movva, N. R. (1989) PepM is an essential gene in *Salmonella* typhimurium, *J. Bacteriol. 171*, 5215−5217.
10. Li, X., and Chang, Y. H. (1995) Amino-terminal protein processing in *Saccharomyces cerevisiae* is an essential function that requires two distinct methionine aminopeptidases, *Proc. Natl. Acad. Sci. U.S.A.* 92, 12357−12361.
11. Ingber, D., Fujita, T., Kishimoto, S., Sudo, K., Kanamaru, T., Brem, H., and Folkman, J. (1990) Synthetic analogues of fumagillin that inhibit angiogenesis and suppress tumour growth, *Nature 348*, 555−557.
12. Griffith, E. C., Su, Z., Turk, B. E., Chen, S., Chang, Y. H., Wu, Z., Biemann, K., and Liu, J. O. (1997) Methionine aminopeptidase (type 2) is the common target for angiogenesis inhibitors AGM-1470 and ovalicin, *Chem. Biol. 4*, 461−471.
13. Sin, N., Meng, L., Wang, M. Q., Wen, J. J., Bornmann, W. G., and Crews, C. M. (1997) The anti-angiogenic agent fumagillin covalently binds and inhibits the methionine aminopeptidase, MetAP-2, *Proc. Natl. Acad. Sci. U.S.A.* 94, 6099−6103.
14. Lowther, W. T., McMillen, D. A., Orville, A. M., and Matthews, B. W. (1998) The anti-angiogenic agent fumagillin covalently modifies a conserved active-site histidine in the *Escherichia coli* methionine aminopeptidase, *Proc. Natl. Acad. Sci. U.S.A.* 95, 12153−12157.
15. Liu, S., Widom, J., Kemp, C. W., Crews, C. M., and Clardy, J. (1998) Structure of human methionine aminopeptidase-2 complexed with fumagillin, *Science 282*, 1324−1327.
16. Zhou, Y., Guo, X. C., Yi, T., Yoshimoto, T., and Pei, D. (2000) Two continuous spectrophotometric assays for methionine aminopeptidase, *Anal. Biochem. 280*, 159−165.
17. Otwinowski, Z., and Minor, W. (1997) Processing of X-ray diffraction data collected in oscillation mode, in *Macromolecular Crystallography*, Part A, Vol. 276, pp 307−326, Academic Press, New York.
18. Kissinger, C. R., Gehlhaar, D. K., and Fogel, D. B. (1999) Rapid automated molecular replacement by evolutionary search, *Acta Crystallogr. D55*, 484−491.
19. Brunger, A. T., Adams, P. D., Clore, G. M., DeLano, W. L., Gros, P., Grosse-Kunstleve, R. W., Jiang, J. S., Kuszewski, J., Nilges, M., Pannu, N. S., Read, R. J., Rice, L. M., Simonson, T., and Warren, G. L. (1998) Crystallography & NMR system: a new software suite for macromolecular structure determination, *Acta Crystallogr. D54*, 905−921.
20. Jones, T. A., Zou, J. Y., Cowan, S. W., and Kjeldgaard, M. (1991) Improved methods for building protein models in electron density maps and the location of errors in these models, *Acta Crystallogr. A47*, 110−119.
21. Sheldrick, G. M., and Schneider, T. R. (1997) SHELXL: high-resolution refinement, *Methods Enzymol. 277*, 277−343.
22. Needleman, S. B., and Wunsch, C. D. (1970) A general method applicable to the search for similarities in the amino acid sequence of two proteins, *J. Mol. Biol. 48*, 443−453.
23. Kleywegt, G. J. (1996) Use of non-crystallographic symmetry in protein structure refinement, *Acta Crystallogr. D52*, 842−857.
24. Barton, G. J. (1993) ALSCRIPT: a tool to format multiple sequence alignments, *Protein Eng. 6*, 37−40.
25. Kraulis, P. J. (1991) MOLSCRIPT: a program to produce both detailed and schematic plots of protein structures, *J. Appl. Crystallogr. 24*, 946−950.

26. DeLano, W. L. (2002) *The PyMOL Molecular Graphics System*, DeLano Scientific, San Carlos, CA, http://www.pymol.org.
27. Li, J. Y., Chen, L. L., Cui, Y. M., Luo, Q. L., Gu, M., Nan, F. J., and Ye, Q. Z. (2004) Characterization of full length and truncated type I human methionine aminopeptidases expressed from *Escherichia coli*, *Biochemistry 43*, 7892−7898.
28. D'Souza V. M., Bennett, B., Copik, A. J., and Holz, R. C. (2000) Divalent metal binding properties of the methionyl aminopeptidase from *Escherichia coli*, *Biochemistry 39*, 3817−3826.
29. Copik, A. J., Swierczek, S. I., Lowther, W. T., D'Souza V. M., Matthews, B. W., and Holz, R. C. (2003) Kinetic and spectroscopic characterization of the H178A methionyl aminopeptidase from *Escherichia coli*, *Biochemistry 42*, 6283−6292.
30. Douangamath, A., Dale, G. E., D'Arcy, A., Almstetter, M., Eckl, R., Frutos-Hoener, A., Henkel, B., Illgen, K., Nerdinger, S., Schulz, H., Mac Sweeney, A., Thormann, M., Treml, A., Pierau, S., Wadman, S., and Oefner, C. (2004) Crystal structures of *Staphylococcus aureus* methionine aminopeptidase complexed with keto heterocycle and aminoketone inhibitors reveal the formation of a tetrahedral intermediate, *J. Med. Chem. 47*, 1325−1328.
31. Schiffmann, R., Heine, A., Klebe, G., and Klein, C. D. (2005) Metal ions as cofactors for the binding of inhibitors to methionine aminopeptidase: a critical view of the relevance of in vitro metalloenzyme assays, *Angew. Chem., Int. Ed. 44*, 3620−3623.
32. Luo, Q., Li, J., Liu, Z., Chen, L., Li, J., Qian, Z., Shen, Q., Li, Y., Lushington, G., Ye, Q., and Nan, F. (2003) Discovery and structural modification of inhibitors of methionine aminopeptidases from *Escherichia coli* and *Saccharomyces cerevisiae*, *J. Med. Chem. 46*, 2631−2640.
33. Holland, D. R., Hausrath, A. C., Juers, D. and Matthews, B. W. (1995) Structural analysis of zinc substitutions in the active site of thermolysin, *Protein Sci. 4*, 1955−1965.
34. Brdlik, C. M., and Crews, C. M. (2004) A single amino acid residue defines the difference in ovalicin sensitivity between type I and type II methionine aminopeptidases, *J. Biol. Chem. 279*, 9475−9480.

BI051691K